J. Fluid Mech. (2009), *vol.* 641, *pp.* 431–440. © Cambridge University Press 2009
doi:10.1017/S0022112009991893

Vortex-induced vibration of a prism in internal flow

M. SÁNCHEZ-SANZ† AND A. VELAZQUEZ

Aerospace Propulsion and Fluid Mechanics Department, School of Aeronautics, Universidad Politécnica de Madrid, Plaza Cardenal Cisneros 3, 28040 Madrid, Spain

(Received 29 May 2009; revised 1 September 2009; accepted 1 September 2009; first published online 13 November 2009)

In this article, we study the influence of solid-to-fluid density ratio m on the type of vortex-induced oscillation of a square section prism placed inside a two-dimensional channel. We assume that the solid body has neither structural damping nor spring restoring force. Accordingly, the prism equation of motion contains only inertia and aerodynamics forces. The problem is considered in the range of Reynolds numbers $Re \in [50\ 200]$ (based on the prism cross-section height h) and channel widths $H = H'/h \in [2.5\ 10]$. We found that, for each Re and H, there is a critical mass ratio m_c that separates two different oscillation regimes. For $m > m_c$, the prism oscillation is periodical and contains a single harmonic. For $m < m_c$, the prism oscillation changes completely and assumes an irregular pattern that is characterized by multiple harmonics that appear to belong to a uniform spectrum. The change from one regime to the other is abrupt and we were not able to observe a transitional regime in which the number of response harmonics grew by finite steps. The value of the critical mass ratio grows along with the Reynolds number and the channel width.

1. Introduction

One of the research lines that are currently being developed within the very broad field of vortex-induced vibrations is the case where no structural restoring force is present. In practice, this situation could be achieved, for example, using air bearings for the experimental set-up mounting (Govardham & Williamson 2002). From the mathematical modelling point of view, this problem is characterized by the fact that no spring constant appears in the equation of motion of the bluff body that oscillates due to vortex shedding. One of the possible applications of a system based on this type of motion is in the area of energy-harvesting microdevices (Sanchez-Sanz, Fernandez & Velazquez 2009).

In the already mentioned work of Govardham & Williamson (2002) the authors point out that, in the flow around a circular cylinder, large-amplitude oscillations appear for values of the ratio between the circular cylinder mass and displaced fluid mass smaller than the critical ratio of 0.54 at the Reynolds number range tested by the authors. Interestingly enough, this oscillation regime of resonance occurs for an infinitely wide span of the normalized velocity, provided that the mass ratio is below the critical value. That study was experimental and the authors analysed the regime in which the Reynolds numbers varied from 4000 up to 22 000. In the

† Email address for correspondence: mario.sanchez@upm.es

https://doi.org/10.1017/S0022112009991893 Published online by Cambridge University Press

low-Reynolds-number regime, Shields, Leonard & Roshko (2001) carried out a numerical study on the oscillations of a circular cylinder at $Re = 100$ immersed in a uniform stream in the limit of zero values of mass, damping and elastic restoring force. Among other findings, the authors noted that flow induced oscillations with amplitudes of the order of the cylinder diameter were possible, even when the spring system was not present. The authors argued that the high-amplitude oscillation was due to the balance between wake vortex forces and inertial forces. Mittal & Singh (2005) found self-excited vibrations at Reynolds numbers as low as $Re = 20$ for an elastically mounted circular cylinder immersed in uniform flow. They found that the mass of the oscillator plays a critical role when determining the ratio of the vortex shedding frequency to the natural frequency of the oscillator. Also, Ryan, Thompson & Hourigan (2005) performed a two-dimensional numerical investigation of the flow-induced vibration of a circular cylinder at low Reynolds numbers in free stream conditions (blockage effects less than 2 %). They identified two different regions of high-amplitude oscillations: one in the range $Re = [40, 95]$ and other for $Re > 180$. In both regimes, the cylinder oscillation frequency was unique.

Concerning a generic discussion on the problem of vortex induced vibration including all relevant parameters, the reader is referred to the reviews of Williamson & Govardhan (2004, 2008) and Sarpkaya (2004).

In this computational investigation we study the transverse vortex-induced vibration of a square cross-section cylinder (prism) in internal flow. We assume that the prism has neither structural damping nor spring restoring force, so that its equation of motion reduces to a balance of inertia and aerodynamics forces. The Reynolds number $Re = \rho_\infty U_\infty h/\mu_\infty$ based on the density and viscosity of the flow ρ_∞ and μ_∞, the mean inlet velocity U_∞ and the cross-section height of the prism h changes in the range 50–200, condition that strengthens the hypothesis of two dimensionality of the flow (Robichaux, Balachandar & Vanka 1999).

The present work is motivated by the findings reported by Sanchez-Sanz *et al.* (2009) in which this configuration was assumed to be coupled to a microelectric generator with the aim of exploring its feasibility as an energy harvesting microdevice. In the present paper there is no coupling to any external generator and we study the influence of the prism-to-fluid density ratio $m = \rho_{solid}/\rho_\infty$ on the prism oscillation observed at different Reynolds numbers. Our work differs from that of other researchers, mainly from that of Ryan *et al.* (2005), in the sense that we consider a prismatic body (not a circular cylinder) and that the blockage ratio plays a critical role in our problem. In what follows, the test problem and the mathematical and numerical models are described first. Next, results are shown and concluding remarks are given.

2. Problem description and mathematical and numerical models

We consider an incompressible fluid flow in a two-dimensional channel around a square section prism that can move freely in the direction transverse to the flow (figure 1). In formulating the problem in non-dimensional form we use the mean inlet velocity U_∞ to scale both horizontal u' and vertical v' velocity components, while h is chosen to scale streamwise x' and transverse y' coordinates. The pressure p' is scaled with the characteristic dynamic pressure $\rho_\infty U_\infty^2$ and the time t' is measured in units of residence time h/U_∞. Introducing the resulting non-dimensional variables $u = u'/u_\infty$, $v = v'/u_\infty$, $p = p'/(\rho_\infty U_\infty^2)$, $x = x'/h$, $y = y'/h$ and $t = U_\infty t'/h$, with

https://doi.org/10.1017/S0022112009991893 Published online by Cambridge University Press

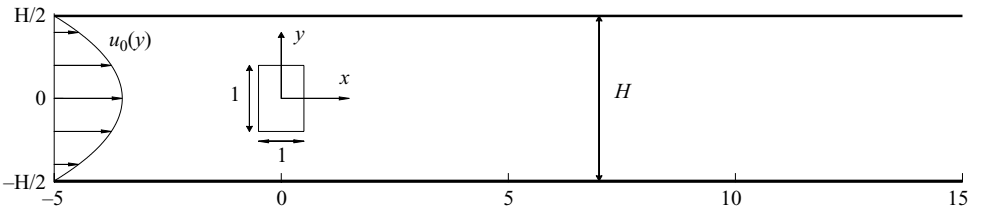


FIGURE 1. Sketch of the configuration investigated.

the primes indicating dimensional variables, the problem reduces to that of integrating

$$\frac{\partial u}{\partial t}+u\frac{\partial u}{\partial x}+v\frac{\partial u}{\partial y}=-\frac{\partial p}{\partial x}+\frac{1}{Re}\left(\frac{\partial^2 u}{\partial x^2}+\frac{\partial^2 u}{\partial y^2}\right), \tag{2.1}$$

$$\frac{\partial v}{\partial t}+u\frac{\partial v}{\partial x}+v\frac{\partial v}{\partial y}=-\frac{\partial p}{\partial y}+\frac{1}{Re}\left(\frac{\partial^2 v}{\partial x^2}+\frac{\partial^2 v}{\partial y^2}\right), \tag{2.2}$$

$$\frac{\partial v}{\partial x}+\frac{\partial v}{\partial y}=0. \tag{2.3}$$

At the inlet section $x=-5$, we assume as boundary conditions a fully developed Poiseuille profile with the pressure computed by solving a discretized version of the x-momentum equation with one-sided derivatives pointing into the computational domain

$$u_0(x)=\frac{6}{4}-6\left(\frac{y}{H}\right)^2, \quad v=0, \quad \frac{\partial p}{\partial x}=-u\frac{\partial u}{\partial x}+\frac{1}{Re}\left(\frac{\partial^2 u}{\partial x^2}+\frac{\partial^2 u}{\partial y^2}\right). \tag{2.4}$$

At the outlet section $x=15$, zero x-derivatives are considered for the velocity components with the pressure computed again from the x-momentum equation with one-sided derivatives

$$\frac{\partial u}{\partial x}=\frac{\partial v}{\partial x}=0, \quad \frac{\partial p}{\partial x}=\frac{1}{Re}\left(\frac{\partial^2 u}{\partial x^2}+\frac{\partial^2 u}{\partial y^2}\right). \tag{2.5}$$

At the fixed and moving solid walls no-slip velocity conditions were imposed: $u=v=0$ at $y=\pm 1.25$ and $u=0$, $v=\mathrm{d}y_c/\mathrm{d}t$ at the prism walls, where $y_c=y_c'/h$ indicates the position of the centre of the cylinder measured from the origin of coordinates. Pressure is obtained by solving the discretized momentum equations with derivatives pointing towards the interior of the computational domain. The channel width $H=H'/h$ is varied to study the effect of the blockage ratio on the flow.

The equation of motion that describes the vortex-induced vibration of the prism in transverse direction y is given by Newton's second law

$$m\frac{\mathrm{d}^2 y_c}{\mathrm{d}t^2}=\frac{1}{2}C_l, \tag{2.6}$$

with $m=\rho_{solid}/\rho_\infty$ being the prism-to-fluid density ratio and $C_l=2F_y/(\rho_\infty u_\infty^2 h)$ the time-dependent lift with F_y the transverse component of the total force induced by the fluid on the prism calculated along its surface Σ

$$F=-\oint_\Sigma p\boldsymbol{n}\,\mathrm{d}\sigma+\frac{1}{Re}\oint_\Sigma \bar{\bar{\tau}}\boldsymbol{n}\,\mathrm{d}\sigma. \tag{2.7}$$

In previous expression, $\boldsymbol{n}$ is the unit length vector normal to the prism surface pointing to the fluid and $\bar{\bar{\tau}}_{xy}=\partial u/\partial y+\partial v/\partial x$.

https://doi.org/10.1017/S0022112009991893 Published online by Cambridge University Press

The computation were started by using a previously calculated velocity field in which the prism remains stationary. At a certain time t_0, the prism is left loose from its original location with zero initial velocity $y_c(t_0) = \mathrm{d}y_c/\mathrm{d}t|_{t=t_0} = 0$.

The numerical integration is performed by using the mixed implicit–explicit relaxation-based pseudo-compressibility formulation proposed by Chorin (1967) and Rogers, Kwak & Kiris (1991) for steady and unsteady problems respectively. According to this method, in order to advance the solution from the real time t^n to the next time step t^{n+1}, an explicit iterative relaxation procedure in the pseudo-time τ is used to solve the set of equations (2.1)–(2.3). Additional derivatives $\partial u/\partial\tau$, $\partial v/\partial\tau$ and $\beta^{-1}\partial p/\partial\tau$ are added to the left-hand side of momentum and continuity equations, with $\beta = 250$ the pseudo-compressibility parameter defined as in Mendez & Velazquez (2004). This method has the advantage of coupling the pressure and velocity fields directly at the same time level so as to generate a set of hyperbolic equations. The resulting artificial waves provide a mechanism to propagate information through the domain and drive pseudo-time derivatives towards zero, thereby satisfying original momentum and continuity equations (2.1)–(2.3). Spatial terms are discretized with a centred second-order accurate scheme while a second-order three-point-backward scheme is used for the temporal terms $\partial\Phi/\partial t|_{i,j}^{n+1} = (1.5\Phi_{i,j}^{n+1} - 2\Phi_{i,j}^{n} + 0.5\Phi_{i,j}^{n-1})/\Delta t$, $\partial\Phi/\partial\tau|_{i,j}^{k+1} = (1.5\Phi_{i,j}^{k+1} - 2\Phi_{i,j}^{k} + 0.5\Phi_{i,j}^{k-1})/\Delta\tau$ where Φ stands for u, v and p. Equations (2.1)–(2.3) are then written at every grid point (x_i, y_j) as

$$\left.\frac{\partial u}{\partial t}\right|_{i,j}^{n+1,k} + \left.\frac{\partial u}{\partial \tau}\right|_{i,j}^{n+1,k+1} = RHS_u\Big|_{i,j}^{n+1,k}, \tag{2.8}$$

$$\left.\frac{\partial v}{\partial t}\right|_{i,j}^{n+1,k} + \left.\frac{\partial v}{\partial \tau}\right|_{i,j}^{n+1,k+1} = RHS_v\Big|_{i,j}^{n+1,k}, \tag{2.9}$$

$$\left.\frac{\partial p}{\partial \tau}\right|_{i,j}^{n+1,k+1} = -\beta\left(\frac{\partial u}{\partial x} + \frac{\partial v}{\partial y}\right)_{i,j}^{n+1,k}, \tag{2.10}$$

where RHS_u and RHS_v include the discretized form of the spatial derivatives of (2.1) and (2.2) respectively. The Navier–Stokes equations are coupled with the equation of motion (2.6) through the lift coefficient C_l. The cylinder position is updated once the pseudo-time iteration has converged by using the immersed boundary method.

The current numerical scheme has been validated by comparing results with the computations of Kelkar & Patankar (1992) at $Re = 100$ and Okajima *et al.* (1997) at $Re = 200$ for confined flows and the experimental measurements of Okajima (1982) with $Re = 200$. Further details of the discretization and series of validations tests cases and sensitivity studies can be found (Mendez & Velazquez 2004; Velazquez, Arias & Mendez 2008; Sanchez-Sanz *et al.* 2009). Temporal and spatial convergence rates of the code have also been checked and they are observed to approach those predicted by the theory. The computational domain presented in figure 1 was described with an uniform grid in both transverse and streamwise direction with spacing $\Delta y = 0.015$, $\Delta x = 0.02$ and a total of 1.66×10^5, 2.49×10^5 and 3.32×10^5 grid points for $H = 2.5$, 3.75 and 5 respectively. On the surface of the cylinder a total of 232 grid points were used to describe its contours. Apart from the above mentioned sensitivity analysis, additional computations were carried out to check the sensibility of the results with the grid by doubling the number of points in both stream and spanwise direction. The maximum differences found between the two meshes were found in the amplitude of the lift coefficient and were reduced to a mere 2 %.

https://doi.org/10.1017/S0022112009991893 Published online by Cambridge University Press

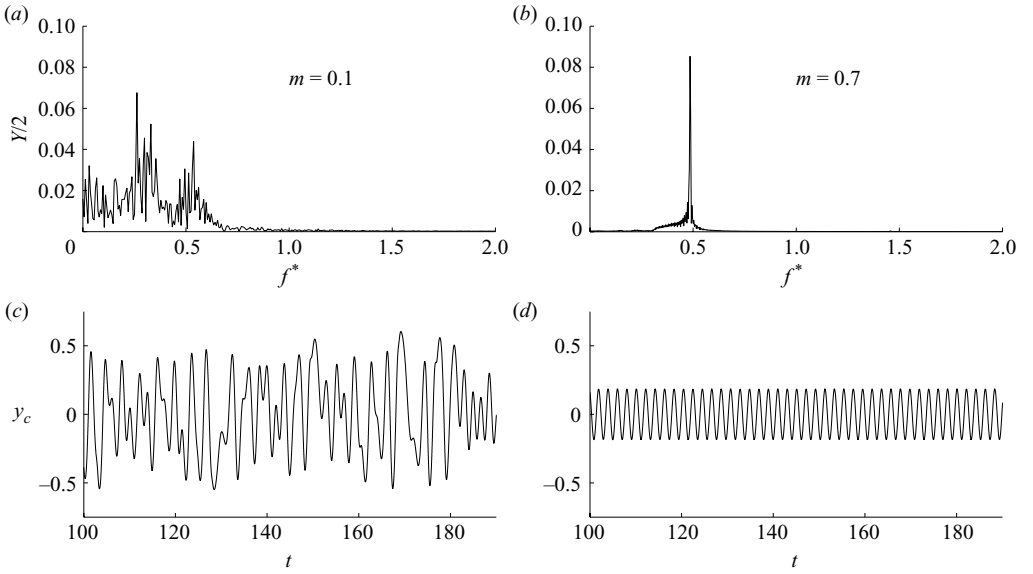


FIGURE 2. Time evolution of the prism location y_c (c, d) and FFT of the displacement (a, b) for $Re = 200$, $H = 2.5$ and $m = 0.1$ and $m = 0.7$. The variable Y in (a) and (b) represents the amount of energy contained in each frequency.

3. Results

3.1. *Oscillatory response*

The set of equations presented in (2.1)–(2.7) depends only on the Reynolds number Re, the density ratio m and the channel width H. To explore their influence we start presenting the solution obtained from the integration of these equations with $Re = 200$ and $H = 2.5$. In figure 2 we show the temporal evolution of the prism location y_c and its fast Fourier transform (FFT)

$$Y(f^*) = \sum_{n=1}^{N} y_c(t_n) \mathrm{e}^{-\mathrm{i}2\pi f^* t_n} \tag{3.1}$$

for density ratios $m = 0.1$ and $m = 0.7$, with N the total number of time steps given in the computation. The non-dimensional frequency number is defined as $f^* = f'h/U_\infty$ with f' the dimensional prism oscillation frequency. The time step chosen during the integration was constant $\Delta t = 10^{-4}$. For $m = 0.7$, the prism oscillates periodically at a neatly defined frequency $f_0^* = 0.49$ determined by the vortices shedding that gives rise to the Kármán street downstream of the cylinder. For this density ratio, all the energy of the spectrum Y is localized in that frequency.

In figure 2 we also present the prism displacement time evolution y_c and its fast Fourier transform for $m = 0.1$. The periodical pattern described for $m = 0.7$ has been abandoned and a completely irregular solution is observed, as can be seen in figures 2(c) and 4(b). The harmonic spectrum in these plots covers the range 0 to 0.6 with similar energies Y contained in every frequency f^*. The maximum oscillation amplitude $y_{c_{max}}$ in this case is much larger that in the case $m = 0.7$ with $y_{c_{max}} = (0.6045, 0.184)$ for $m = (0.1, 0.7)$ respectively. This trend continues as m grows and leads, in the limit $m \to \infty$, to a solution completely equivalent to that of the

https://doi.org/10.1017/S0022112009991893 Published online by Cambridge University Press

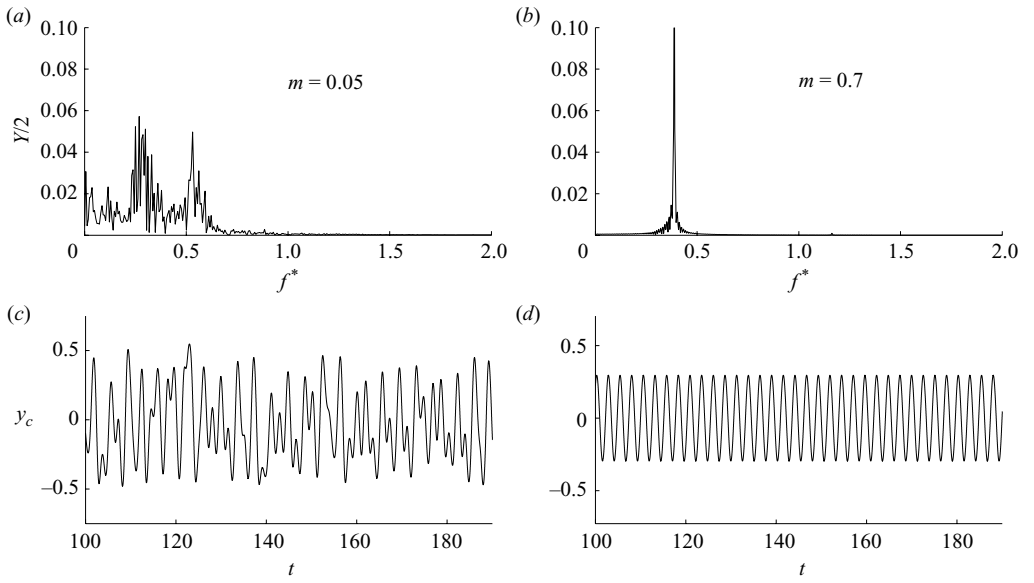


FIGURE 3. Time evolution of the prism location y_c (c, d) and FFT of the displacement (a, b) for $Re = 50$, $H = 2.5$ and $m = 0.05$ and $m = 0.7$. The variable Y in (a) and (b) represents the amount of energy contained in each frequency.

stationary prism in which the oscillation amplitude is zero and the non-dimensional vortex detachment frequency is $S_t = f'_{vs}h/U_\infty \sim 0.412$.

A similar type of behaviour has been observed for $Re = 50$. In figure 3 we show the results obtained (displacement time history and FFT) at this lower Reynolds number for $m = 0.05$ and $m = 0.7$. For $m > 0.07$ the oscillation was found to have a regular pattern. The behaviour of the solution observed for the different Re suggests the existence of a critical density ratio m_c separating the unique-frequency oscillation regime from the highly irregular one.

The relation between the oscillation amplitudes in the regular oscillation regime $m > m_c$ can be easily obtained from the prism motion equation (2.6). Assuming that the aerodynamical forces take the form $C_l = F_0 \sin(2\pi S_t t - \theta)$, with θ a certain phase angle, F_0 the force amplitude and S_t the non-dimensional frequency of vortex shedding. The position of the cylinder can, therefore, be obtained from the integration of (2.6) to give $y_c = -C_{Re} \sin(2\pi f^* t)$ with $C_{Re} = F_0/[2m(2\pi f^*)^2]$ and $f^* = S_t$. For a certain density ratio m, we can write

$$K = \frac{C_{Re=50}}{C_{Re=200}} = \frac{F_{0,Re=50}}{F_{0,Re=200}} \left(\frac{f^*_{Re=200}}{f^*_{Re=50}} \right)^2. \tag{3.2}$$

From the numerical integration we obtain non-dimensional frequency numbers $f^* = (0.488, 0.380)$, force amplitudes $F_0 = (2.809, 2.710)$ and maximum oscillation amplitudes $y_{c_{max}} = (0.184, 0.296)$ for $m = 0.7$, $H = 2.5$ and $Re = (200, 50)$ respectively. The ratio between both numerical amplitudes gives $K = 1.608$, which compares well with the value of $K = 1.591$ calculated from (3.2). From the numerical results, small differences of around 4 % are observed in the force amplitude for $Re = 50$ and $Re = 200$. Based on this, we could assume F_0 constant in the range of Reynolds numbers considered and write (3.2) as $K = (f^*_{Re=200}/f^*_{Re=50})^2$ to get $K = 1.649$. This simplification works relatively well since, for $m > m_c$, transverse forces are mainly

https://doi.org/10.1017/S0022112009991893 Published online by Cambridge University Press

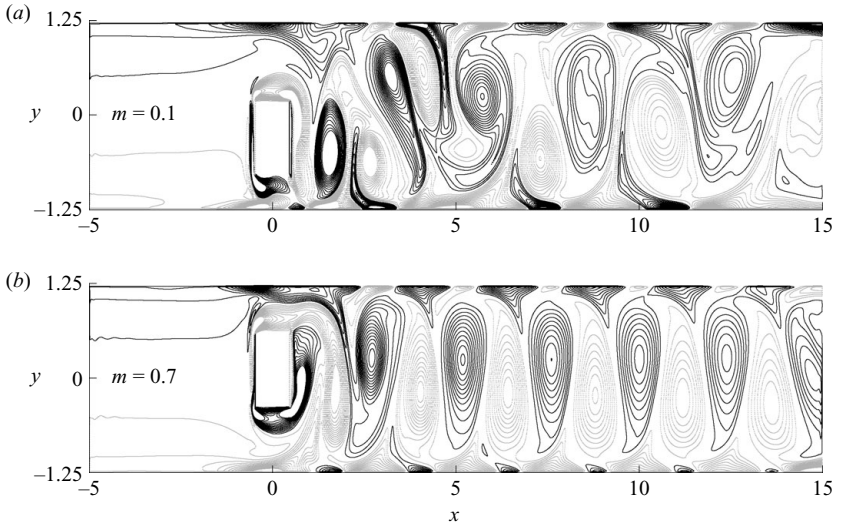


FIGURE 4. Vorticity $\omega = \partial v/\partial x - \partial u/\partial y$ isocontours obtained for $Re = 200$, $H = 2.5$ and $t = 258$ with $m = 0.1$ (a) and $m = 0.7$ (b) in the range $\omega \in [-15,\ 15]$ with $\Delta\omega = 1$. Negative vorticity is plotted in grey while positive vorticity is in black.

created by pressure gradients, with a contribution of order $O(Re^{-1})$ from the viscous terms that becomes increasingly important as Re reduces.

3.2. *Critical mass* m_c

A continuous reduction of an initially large density ratio m reveals an unexpected feature related to the periodicity of the prism oscillation. The unique-frequency oscillation behaviour holds for decreasing m until the condition $m = m_c$ is satisfied. For this density ratio, the character of the solution changes abruptly and the time evolution of the cylinder location changes from the smooth periodical oscillation to a completely irregular pattern as shown in figures 2–4.

To clarify this point, we performed a series of numerical simulations changing the density ratio from $m = 2$ down to 0.1. The results obtained are presented in figure 5 where the peaks of the oscillation frequency spectrum are shown for each mass ratio. For sufficiently large density ratios $m > m_c$, the non-dimensional frequency f^* is single-peaked and its value increases as the density ratio decreases. Then, for $m = m_c$ the system suddenly enters into an unstable mode and the oscillation frequency goes from a well-defined value to a nearly continuum frequency spectrum indicating that the prism is moving following a strongly irregular pattern. This abrupt change in the solution defines the critical density ratio m_c.

In figure 5 the oscillation frequency is plotted versus the density ratio for $Re = 50$ and 200 and $H = 2.5$. In both cases f^* is well defined until a bifurcation is observed in the plot for a certain $m = m_c$. From the numerical solution we get $m_c \simeq (0.31, 0.07)$ for $Re = (200, 50)$ respectively. The dependency of m_c with the Reynolds defines the map of solutions plotted in figure 6(a).

In all Reynolds numbers considered we tried to discern whether the transition from the regular to the irregular regime was abrupt or period doubling could be observed. In this regard, we have to say that period doubling has been only observed for $Re = 200$ in a narrow range of density ratio $m \in [0.31\ \ 0.29]$ in which the oscillation

https://doi.org/10.1017/S0022112009991893 Published online by Cambridge University Press

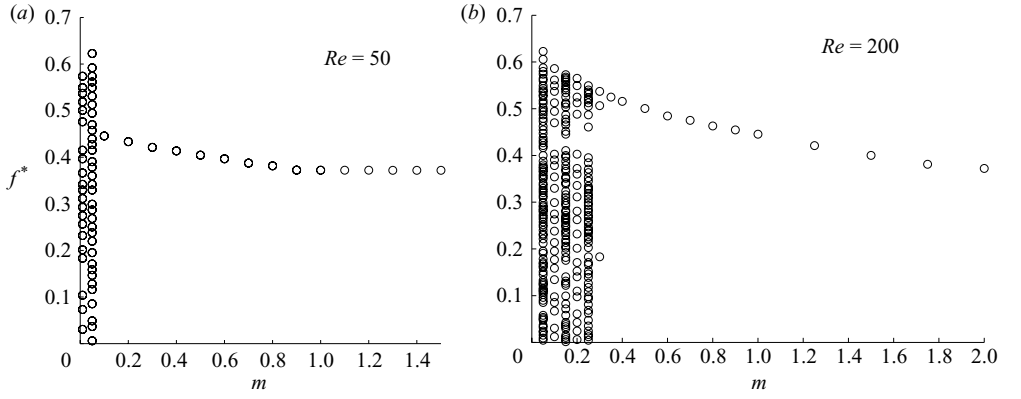


FIGURE 5. Peaks in the oscillation frequency spectrum as a function of the mass ratio m for $Re = 50$ (a) and $Re = 200$ (b) and $H = 2.5$.

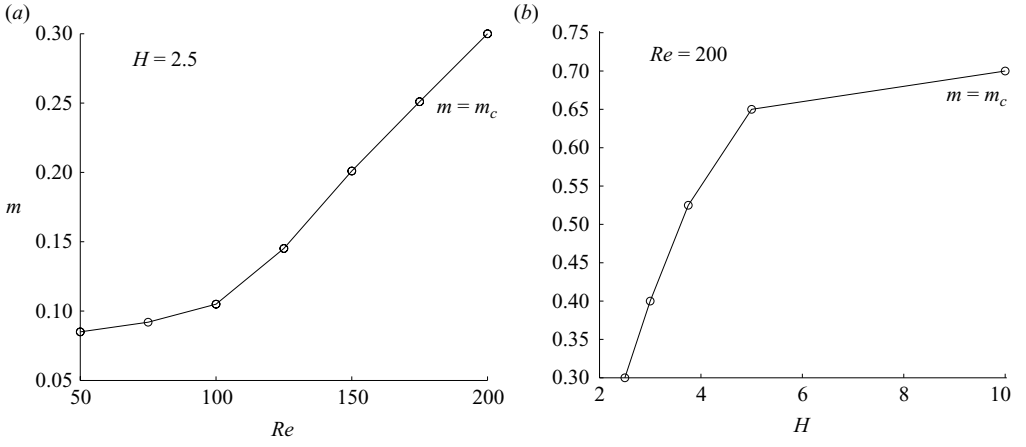


FIGURE 6. Critical mass m_c as a function of the Reynolds number ($H = 2.5$) (a), and of the blockage ratio ($Re = 200$) (b).

Strouhal number stop being unique and the spectrum showed progressively increasing oscillation harmonics.

3.2.1. *Blockage ratio*

Another important parameter that affects the problem behaviour is the channel width H. To study this effect, we have performed an additional series of computations to identify, for different values of H, the critical mass ratio that separates the two oscillation regimes at $Re = 200$. The results are summarized in figure 6(b), where it could be observed that m_c tends to increase for larger values of H. From the point of view of applications, if alternatives are sought to increase mixing, the conclusion from this parametric study is that the combination of a strong blockage and a light body favours this effect which, incidentally, goes in the direction of making the system more compact and lighter.

3.3. *Pressure drop*

A final question is related to the larger pressure drop that occurs along the channel because of the prism motion. In figure 7 we show the time evolution of the

https://doi.org/10.1017/S0022112009991893 Published online by Cambridge University Press

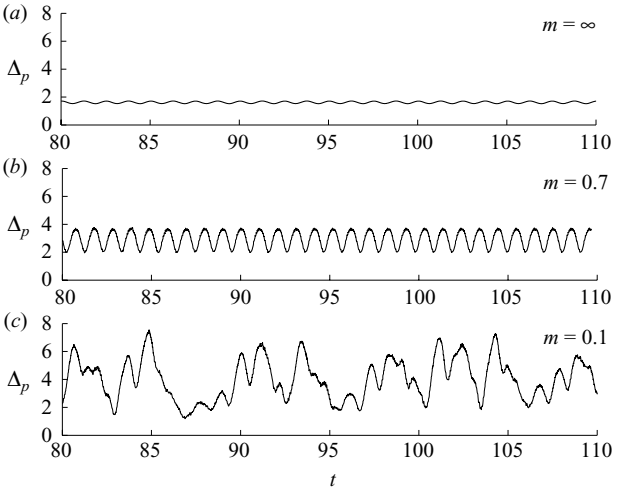


FIGURE 7. Pressure drop with $Re = 200$ and $H = 2.5$ for the steady prism $m = \infty$ (a) and with moving prism with $m = 0.7$ (b) and $m = 0.1$ (c).

space-average pressure drop $\Delta p(t) = -H^{-1} \int_{-H/2}^{H/2} (p(x_R) - p(x_F))\, \mathrm{d}y$ between the section located just before $x_F = -0.5$ and after the prism $x_R = 0.5$ for $Re = 200$ and $H = 2.5$ in three situations: stationary prism $m \to \infty$ (figure 7a), oscillation with $m = 0.7$ (figure 7b) and oscillation with $m = 0.1$ (figure 7c).

As expected, the pressure drop behaves following a pattern similar to that of the prism oscillation. Also, it is to be noted that the time averaged values of this pressure drop (related to the power of the pump needed to propel the fluid) $\overline{\Delta p} = (t_2 - t_1)^{-1} \int_{t_1}^{t_2} \Delta p \, \mathrm{d}t$ are $\overline{\Delta p} = (1.611, 2.923, 3.963)$ for $m = (\infty, 0.7, 0.1)$ respectively. This increment in the pressure drop is easy to understand if we remember that the prism is oscillating. The effective blockage ratio for the stationary prism $m = \infty$ is $1/H = 0.4$ much smaller than that of the moving cylinder $2(y_{c_{max}} + 0.5)/H = (0.5475, 0.880)$ for $m = (0.7, 0.1)$. Therefore, the rest of the channel width is occupied by a high-level vorticity region that constraints the space through where the fluid can flow downstream.

4. Concluding remarks

We found that in the vortex induced motion of a prism in internal flow with neither damping nor restoring force at low Reynolds number, two different regimes are present. These two regimes are characterized by the oscillation pattern that is regular (one frequency) above certain critical mass and becomes highly irregular (near continuum spectrum of harmonics) below that critical value. Transition from one regime to the other is abrupt and this fact opens up some possibilities when thinking about practical applications of the system being described (that could be easily materialized using standard micromanufacturing facilities). For example, the oscillation pattern could be used to detect changes in the flow Reynolds number, either because of changes in velocity or temperature (for instance, water Reynolds number threefold for temperature changes in the range 20 °C–80 °C due to kinematic viscosity variations). It was also found that the oscillation pattern strongly influences both the time evolution of the pressure drop and its time-averaged value that is related to the power needed by the pump to propel the fluid.

https://doi.org/10.1017/S0022112009991893 Published online by Cambridge University Press

The different oscillation flow patterns also suggest the idea of using this system to promote mixing at these low Reynolds numbers. For example, if one were to promote heat transfer inside a microchannel, the results presented in this article could be used to design a kind of moving vortex promoter that would enhance downstream mixing; albeit at a higher pumping cost because the space–time averaged pressured drop is larger for values of m below m_c. This is the subject of ongoing research.

The authors want to acknowledge support from project DPI-2009-07591 of Plan Nacional de I+D+i of the Spanish Ministry of Science and Innovation.

REFERENCES

Chorin, A. J. 1967 A numerical method for solving incompressible viscous flow problems. *J. Comput. Phys.* **2**, 12–26

Govardham, R. & Williamson, C. H. K. 2002 Resonance forever: existence of a critical mass an infinite regime of resonance in vortex-induced vibration. *J. Fluid Mech.* **473**, 147–166.

Kelkar, K. M. & Patankar, S. V. 1992 Numerical prediction of vortex shedding behind a square cylinder. *Intl J. Numer. Methods Fluids* **14**, 327–341.

Mendez, B. & Velazquez, A. 2004 Finite point solver for the simulation of two-dimensional laminar, incompressible, unsteady flows. *Comput. Methods Appl. Mech. Engng* **193**, 825–848.

Mittal, S. & Singh, S. 2005 Vortex-induced vibrations at subcritical Re. *J. Fluid Mech* **534**, 185–194.

Okajima, A. 1982 Strouhal numbers of rectangular cylinders. *J. Fluid Mech.* **123**, 379–398.

Okajima, A., Yi, D., Sakuda, A. & Nakano, T. 1997 Numerical study of blockage effects on aerodynamics characteristics of an oscillating rectangular cylinder. *J. Wind Engng Ind. Aerodyn* **67–68**, 91–102.

Robichaux, J., Balachandar, S. & Vanka, S. P. 1999 Three-dimensional Floquet instability of the wake of square cylinder. *Phys. Fluids* **11**, 560–578.

Rogers, S. E., Kwak, D. & Kiris, C. 1991 Numerical solution of the incompressible Navier–Stokes equations for steady-state and time-dependent problems. *AIAA J.* **29** (4), 603–610.

Ryan, K., Thompson, M. C. & Hourigan, K. 2005 Variation in the critical mass ratio of a freely oscillating cylinder as a function of Reynolds number. *Phys. Fluids* **17**, 038106.

Sanchez-Sanz, M., Fernandez, B. & Velazquez, A. 2009 Energy-harvesting microresonator based on the forces generated by the Kármán street around a rectangular prism. *J. Microelectromech. Syst.* **18**, 449–457.

Sarpkaya, T. 2004 A critical review of the intrinsic nature of vortex-induced vibrations. *J. Fluids Struct.* **19**, 389–447.

Shiels, D., Leonard, A. & Roshko, A. 2001 Flow induced vibration of a circular cylinder at limiting structural parameters. *J. Fluids Struct.* **15**, 3–21.

Velazquez, A., Arias, J. R. & Mendez, B. 2008 Laminar heat transfer enhancement downstream of a backward facing step by using a pulsating flow. *Intl J. Heat Mass Transfer* **51**, 2075–2089.

Williamson, C. H. K. & Govardhan, R. 2004 Vortex induced vibrations. *Annu. Rev. Fluid Mech.* **36**, 413–455.

Williamson, C. H. K. & Govardhan, R. 2008 A brief review of recent results in vortex-induced vibrations. *J. Wind Engng Ind. Aerodyn.* **96**, 713–735.

https://doi.org/10.1017/S0022112009991893 Published online by Cambridge University Press